NANO LETTERS

pubs.acs.org/NanoLett

Letter

Probing the Limits to Near-Field Heat Transfer Enhancements in Phonon-Polaritonic Materials

Rohith Mittapally, Ju Won Lim, Lang Zhang, Owen D. Miller,* Pramod Reddy,* and Edgar Meyhofer*

Cite This: *Nano Lett.* 2023, 23, 2187−2194

Read Online

ACCESS | Metrics & More | Article Recommendations | Supporting Information

ABSTRACT: Near-field radiative heat transfer (NFRHT) arises between objects separated by nanoscale gaps and leads to dramatic enhancements in heat transfer rates compared to the far-field. Recent experiments have provided first insights into these enhancements, especially using silicon dioxide (SiO_2) surfaces, which support surface phonon polaritons (SPhP). Yet, theoretical analysis suggests that SPhPs in SiO_2 occur at frequencies far higher than optimal. Here, we first show theoretically that SPhP-mediated NFRHT, at room temperature, can be 5-fold larger than that of SiO_2, for materials that support SPhPs closer to an optimal frequency of 67 meV. Next, we experimentally demonstrate that MgF_2 and Al_2O_3 closely approach this limit. Specifically, we demonstrate that near-field thermal conductance between MgF_2 plates separated by 50 nm approaches within nearly 50% of the global SPhP bound. These findings lay the foundation for exploring the limits to radiative heat transfer rates at the nanoscale.

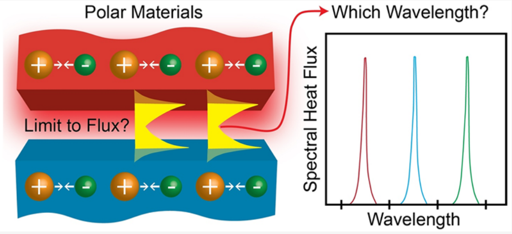

KEYWORDS: *near-field radiative heat transfer, surface phonon polaritons, dielectric materials, thermal radiation, magnesium fluoride, silicon dioxide*

Near-field radiative heat transfer (NFRHT) describes the transfer of thermal energy between objects separated by distances smaller than the dominant wavelength of thermal radiation. In recent years this area has attracted much interest,[1−3] because at nanometer separations the radiative energy transfer between objects can readily exceed tens of kW m^{-2} which offers significant potential for future applications in energy transport and conversion, including in thermo-photovoltaics,[4−7] photonic refrigeration,[8,9] thermal management,[10−12] and heat-assisted magnetic recording.[13] Large radiative heat fluxes arise in the near-field—well above the blackbody limit that sets the upper bound to far-field radiative heat transfer (RHT)—as contributions from surface waves, such as surface plasmon polaritons (SPPs) and surface phonon polaritons (SPhPs) or from the evanescent tails of guided modes, dramatically enhance heat transfer rates (Figure 1A). Moreover, the density of evanescent channels increases quadratically with their surface-parallel wavevector *k*, offering significantly increasing numbers of energy-transport channels with increasing *k*. Therefore, as the gap size between objects is reduced to the nanoscale, surface waves enable access to increasingly high-*k* channels, leading to dramatic increases in RHT. In contrast, in far-field RHT, the gaps between the surfaces are much larger than the penetration depth of the evanescent modes and hence only propagating waves contribute to energy transport in this regime. Following significant theoretical and computational efforts (see for example refs 14−18), experimental studies leveraging detailed measurements on a few select dielectric and metallic materials were finally able to independently confirm the validity of the framework of fluctuational electrodynamics[10,19−26]), which is now broadly used to study various transport mechanisms and materials in NFRHT.

However, what has not been addressed yet with regard to the fundamental understanding of NFRHT is the important question: Is it feasible to develop a theoretical framework that predicts, analogous to the blackbody limit in far-field RHT, the maximum NFRHT flux for any given class of materials at a given gap size? The focus of this letter is to first address this question and to develop a new theoretical framework that explores limits to NFRHT across all materials that support SPhP resonances. Next, building upon insights from this framework, we identify Al_2O_3 and MgF_2 as materials that support SPhP frequencies close to or almost exactly coinciding with the optimal frequency identified by our theory. Finally, we leverage state-of-the-art experimental approaches to directly characterize the NFRHT rates of Al_2O_3 and MgF_2 for gap sizes ranging from 42 nm to 7 μm. Our experimental findings establish the validity of our model and show that MgF_2 closely approaches this upper NFRHT bound.

We begin by noting that early computational studies suggested that SiO_2 is an attractive material and a well-suited

Received: December 2, 2022
Revised: February 28, 2023
Published: March 8, 2023

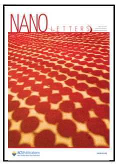

https://doi.org/10.1021/acs.nanolett.2c04735
Nano Lett. 2023, 23, 2187−2194

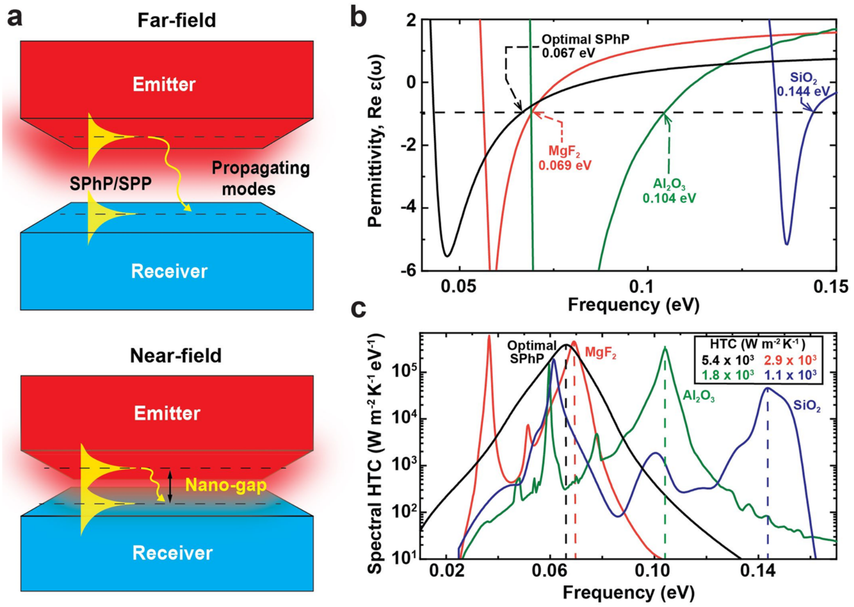

Figure 1. Schematic description and theoretical basis for enhancement of NFRHT. (a) Illustration of the modes contributing to radiative heat transfer (RHT) between a hot emitter and a cold receiver. In the near-field, surface modes, such as surface phonon polaritons (SPhPs) and surface plasmon polaritons (SPPs), contribute to a large RHT. (b) Real part of the dielectric functions for SiO_2 (solid blue line), MgF_2 (solid orange line), and Al_2O_3 (solid green line), the materials probed in this work along with the real part of the dielectric function for an optimal material (solid black line). We note that to date SiO_2 has the highest reported near-field heat-transfer coefficients (HTCs), and its optical phonon modes support SPhPs near 144 meV that nearly align with the conventional Wien frequency (128 meV). Yet the optimal frequency is much smaller due to near-field densities of states, and the optimal SPhP-mediated HTC (black) occurs for materials with $\varepsilon \approx -1$ at 67 meV. In contrast to SiO_2, Al_2O_3 supports SPhPs near 104 meV, while MgF_2 supports SPhPs near 69 meV, almost exactly optimal (vertical transitions with negligible contribution to HTC are removed for clarity). (c) Spectral HTC at a 50 nm gap size for MgF_2, Al_2O_3, SiO_2, and the theoretically optimal SPhP material. The values in the inset show that MgF_2 theoretically achieves the highest HTC at any near-field gap size, reaching within 54% of the SPhP upper bound.

platform to achieve large enhancements in NFRHT, because SiO_2 supports SPhPs at ∼144 meV (10 μm free-space wavelength), very near the optimal thermal frequency (∼128 meV) predicted by Wien's Law at a temperature of 300 K. Recent experiments with SiO_2 surfaces[19,21,24] have tested these predictions and shown significant enhancements relative to far-field RHT. However, from a fundamental viewpoint a key unanswered question is if other material systems can support even larger enhancements in NFRHT. A variety of computational works demonstrated further possible enhancements in systems ranging from ideal Drude- or Drude−Lorentz-model materials,[27−29] to metasurfaces,[30−33] and thin-film and multilayer[34−36] structures. For example, a study[32] that explored nanostructured doped-Si surfaces predicted an enhancement that is ∼3 times higher than that observed for SiO_2. The largest potential NFRHT rates that have been discussed up to this point are based on the fundamental upper limits associated with conservation laws,[37,38] yet those limits are not constructive, as they do not identify real-world structures and may well not be practically achievable. Some of us have suggested,[39] by computationally exploring the space of all bodies obeying causal susceptibilities, that 5-fold enhancements in NFRHT, over that of SiO_2, should be possible and predicted that certain conducting oxides and aluminum and titanium nitrides may approach this limit. However, the material systems suggested for this approach require dopants at unusually low concentrations, which are not readily available for experimental verification as very few other applications call for plasmonic resonances at such long wavelengths.

A related question that one can ask is the following: What is the largest possible NFRHT conductance achievable in materials where NFRHT is mediated by a SPhP resonance between plane-parallel surfaces? We answer this question in a general way by adapting an approach some of us developed in ref 39. The key idea is that causality ensures that any passive, local material can be represented as an infinite sum of Drude-Lorentz oscillators, with the coefficients ("oscillator strengths") as the only degrees of freedom.[39,40] Applied to the question of maximum NFRHT, it was found in ref 39 that optimizing over arbitrarily large numbers of oscillators led to a single Drude-like oscillator, with all of its oscillator strength concentrated at zero oscillator frequency. Such materials are expected to exhibit HTC coefficients as large as 9200 W m^{-2} K^{-1} at 50 nm gap sizes, but they would require a free-electron-like response at mid-IR frequencies that is difficult to achieve in either natural or doped materials.

To apply the causality-based optimization framework to the question of maximal NFRHT mediated by SPhP resonances, we need to incorporate the distinguishing features of phonon-polaritonic materials. Toward this goal, we utilize the empirical fact that the ratio of the transverse to longitudinal frequencies of the optical phonon modes shows little variation across a broad range of materials and, for many common materials (see Supporting Information for more details), is bounded above by $\omega_{LO}/\omega_{TO} \leq 2$. The square of this ratio forms the basis for the Lyddane−Sachs−Teller (LST) relation, which relates the ratio to zero- and high-frequency properties of the optical-phonon contributions to the dielectric function.[41,42] We impose this ratio as a constraint on the many-oscillator representation, as detailed in the Supporting Information, which constrains the allowable oscillator strengths across all oscillator frequencies. We find that, independent of the number of oscillators

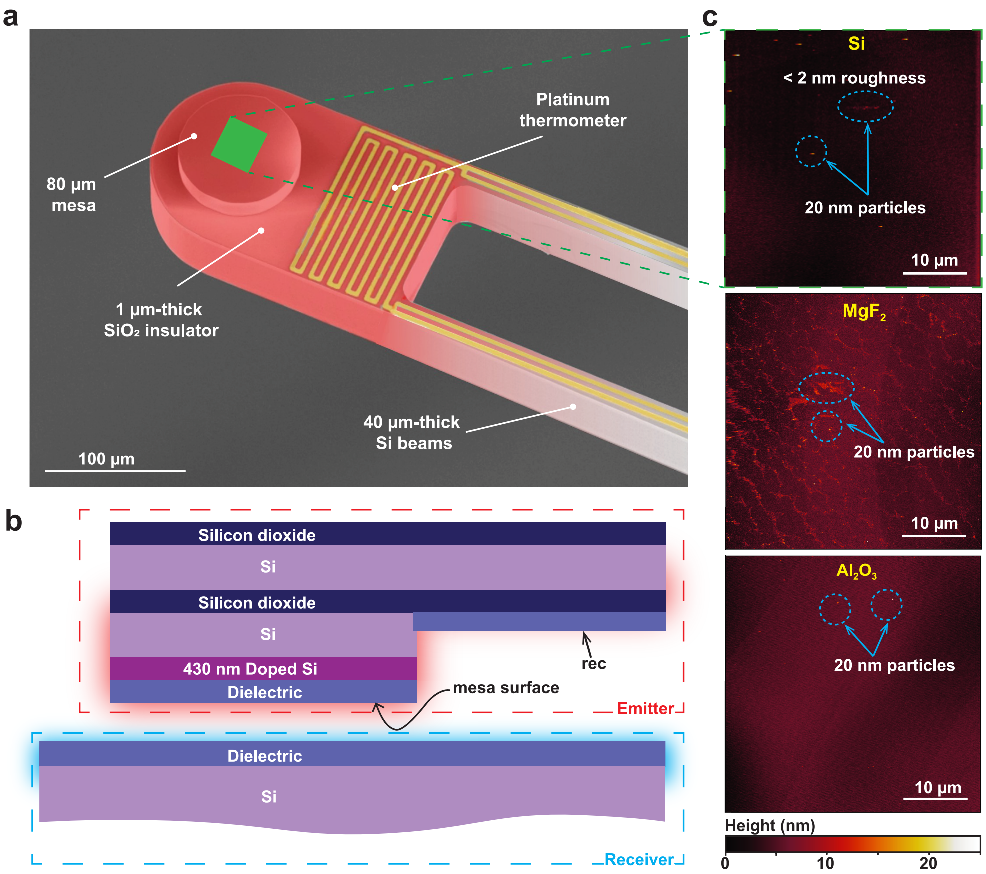

Figure 2. Description of the device structures and their surface characteristics. (a) False-colored scanning electron micrograph of the microfabricated calorimeter depicting the flat and smooth mesa and the island suspended by two thick silicon beams. The platinum thermometer, electrically isolated from the mesa, acts as a heater and a thermometer. (b) Schematic depicting the different layers in the emitter (with a recessed region "rec") and receiver. (c) Atomic force microscopy scans of the mesa surface. The first panel shows an as-fabricated mesa (40×40 μm^2 area marked as green region in (a)), indicating RMS roughness < 2 nm. The second and third panels show mesa surfaces coated with films of MgF_2 and Al_2O_3, respectively. The surface RMS roughness is below 5 nm, with a small number of ~20 nm-sized particles.

included in the optimization, the optimal solution converges to a single lossy oscillator, but with a nonzero oscillator frequency. By requiring the satisfaction of the Lyddane−Sachs−Teller relation, a new globally optimal HTC value emerges. At 300 K the real part of the optimal dielectric function in the vicinity of the optical phonon would then be that depicted by the solid black line of Figure 1B; the key data point is that the frequency at which Re $\varepsilon(\omega)$ crosses -1 is about 67 meV, which also aligns well with the peak of the spectral heat transfer coefficient (HTC), as shown in Figure 1C. The total HTC of this optimal SPhP material at a gap size of 50 nm is ~5400 W m^{-2} K^{-1}, about 5 times larger than that of SiO_2. At higher temperatures, the optimal oscillator frequencies increase linearly with temperature, as does the optimal HTC rate. Section 10 and Figure S9 in the SI discuss and show the linear temperature dependencies in more detail.

Our analysis reveals that the shortcoming of SiO_2 is that its strongest optical-phonon-mode response occurs at much larger frequencies (~144 meV) than optimal. Yet, there are other materials with a nearly ideal response. We highlight two materials: alumina (Al_2O_3), which has a large contribution at about 104 meV as well as a nontrivial response near 50 meV, and MgF_2, whose strongest response occurs at 69 meV, very near the optimal frequency. The superior natures of Al_2O_3 and MgF_2 compared to SiO_2 are apparent from their dielectric functions, as shown in Figure 1B, which results in their larger spectral HTC values as depicted in Figure 1C. MgF_2, in particular, has a spectral HTC that nearly overlaps with the ideal phonon-mediated HTC spectrum. Theory suggests that Al_2O_3 and MgF_2 should exhibit conductance values of 1800 W m^{-2} K^{-1} and 2900 W m^{-2} K^{-1}, at gaps of 50 nm, which would approach within 33% and 54% of the global SPhP bound, respectively.

In order to explore if the theoretical bounds described above can actually be accomplished using materials like Al_2O_3 and MgF_2, we employ an experimental platform that combines high-resolution and stiff calorimetric microdevices[4,8,10] with a custom-built nanopositioner[43] that allows precise alignment and positioning of calorimetric devices, making possible gap sizes below 100 nm between planar surfaces of the microdevices. The microdevices feature an 80 μm-diameter circular mesa that extends 15 μm from the rest of the device (see Figure 2A, Supporting Information and Figure S1 for details of the fabrication). A thin-film serpentine platinum line integrated into the suspended island is used in a modulated-thermometry measurement scheme.[44] The island is suspended from the substrate by two thick beams (40 μm in thickness, 13 μm in width, and 550 μm in length resulting in a thermal conductance (G_{dev}) of ~260 μW/K; see Supporting Information). A 1 μm-thick SiO_2 layer provides the electrical isolation between the platinum thermometer and the mesa. The schematic in Figure 2B shows the different layers of the

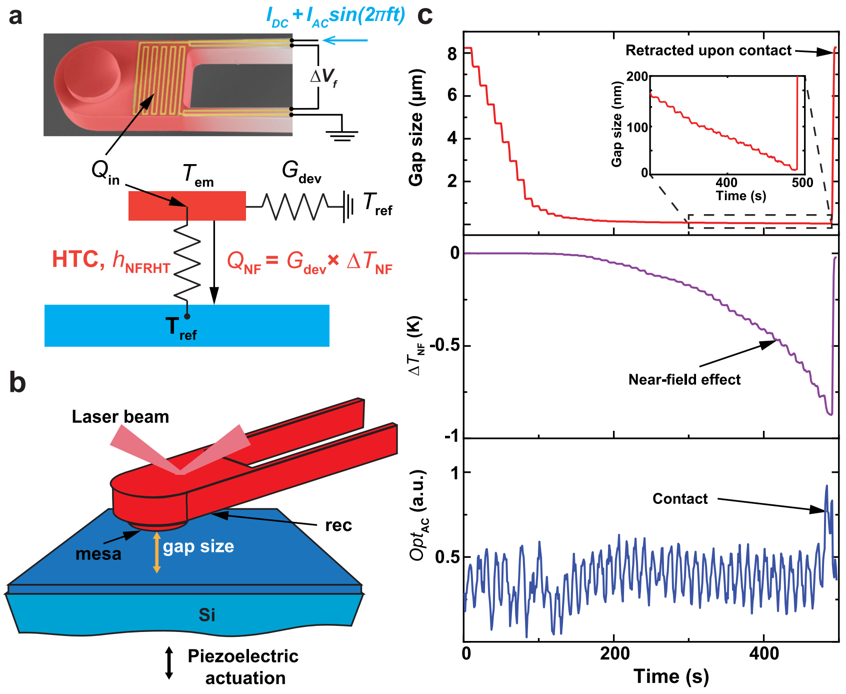

Figure 3. Description of the measurement scheme and representative experimental data. (a) Thermal model, showing temperatures at the three nodes, as well as corresponding thermal resistances, conductances, and heat input. A current equal to $I_{DC} + I_{AC}\sin(2\pi ft)$ is passed through the serpentine resistor (as shown in the false-colored scanning electron micrograph), and the resulting amplitude of voltage signal ΔV_f is continuously measured. T_{ref} is the temperature of the substrate and cold receiver, G_{dev} is the thermal conductance of the emitter, T_{em} is the temperature of the emitter, Q_{in} is the power dissipated in the Pt resistor, Q_{NF} is the radiative heat transfer due to near-field effects, and h_{NFRHT} is the radiative heat transfer coefficient. (b) Schematic of the assembled devices in a near-field experiment, depicting the emitter placed above a receiver device. The gap size is controlled using a piezoelectric actuator on the receiver side. Contact with the receiver is monitored by reflecting a laser beam off the backside of the emitter. The recessed region (rec) emits far-field radiation only that is accounted for in the theoretical calculations. (c) Real-time sample data depicting an approach between a MgF_2-coated receiver a MgF_2-coated emitter that was heated by 12 K. The top panel shows the displacement steps of the emitter before contact. Large steps are taken initially, and smaller steps of ∼2 nm are taken close to contact. The inset shows the steps taken in the last 200 nm. The middle panel displays the corresponding temperature changes of the emitter. Large changes are observed in the last few hundred nanometers, indicating a steep increase in near-field-based heat flux from the hot emitter to the cold receiver for small gap sizes. The third panel depicts the optical signal, which remains noise-limited until contact occurs between the two devices.

microfabricated emitter structure. The mesa surface, as fabricated, is extremely flat and smooth, with an RMS roughness < 2 nm (Figure 2C, top panel). Polar dielectrics, such as MgF_2 and Al_2O_3, are deposited on these microdevices using electron beam evaporation and atomic layer deposition techniques, respectively. The RMS roughness of the deposited surface is ∼3−5 nm. There are a small number of ∼20 nm-sized particles observed on the dielectric films (Figure 2C). Based on the size of these particles and the slight misalignment in parallelization between the two surfaces, we estimate the minimum gap size to be 40 nm.

The receiver is held at ambient temperature (not heated or cooled) and is a pristine, large area (1 cm × 1 cm sized) silicon substrate (Figure 2B) coated with the identical dielectric (MgF_2 or Al_2O_3) of suitable thickness (85 or 195 nm, respectively). In general, thicker films more closely approximate a semi-finite surface but are more prone to having a larger roughness during deposition, which prevents accomplishing NFRHT measurements at small gaps. Thus, the thicknesses employed in our experiments represent a trade-off between these two competing factors. The emitter and receiver devices are precisely aligned in the nanopositioner (see our previous works[7,8,10,19,21] for detailed procedures), after which the whole assembly is placed in a chamber held at a pressure of $\sim 5 \times 10^{-7}$ Torr to suppress conductive and convective heat transfer. The platinum serpentine integrated into the emitter works as both a heater and a thermometer. Upon supplying a current $I(t)$ consisting of AC and DC components (Figure 3A), $I(t) = I_{DC} + I_{AC}\sin 2\pi ft$, there is heat dissipation in the probe given by $Q_{in} = I_{DC}^2 R + I_{AC}^2 R/2 + 2I_{AC}I_{DC}R\sin(2\pi ft) - I_{AC}^2 R\cos(4\pi ft)/2$, where R is the Pt resistance. Since the frequency of modulation, f, is chosen to be 495 Hz, much higher than the thermal cutoff frequency of the emitter (see Supporting Information for frequency response of the emitter), the DC temperature rise is proportional to $I_{DC}^2 R + I_{AC}^2 R/2$. The emitter temperature is simultaneously monitored by measuring the voltage fluctuations at $f(\Delta V_f)$, via a lock-in detection scheme resulting in measurement of the temperature changes of the emitter (ΔT_{NF}, see Supporting Information and ref 44 for the measurement details). The total radiative heat transfer Q_{NFRHT} is then calculated based on the thermal resistance network, which is shown in Figure 3A along with the corresponding thermal conductances and temperatures. In the far-field, $Q_{in} = G_{dev} \times \Delta T_{ref}$, where $\Delta T_{ref} = T_{em,i} - T_{ref}$, $T_{em,i}$ is the initial temperature of the emitter and T_{ref} is the temperature of the substrate (300 K). As the gap size is reduced, the emitter temperature reduces by ΔT_{NF} to $T_{em,2}$. Thus, the gap-dependent heat flux change, Q_{NF}, corresponding to this temperature change ΔT_{NF}, is given by $Q_{NF} = G_{dev} \times \Delta T_{NF}$. The total radiative heat flux is then calculated as the sum of the measured heat change (Q_{NF}) and a calculated far-field heat transfer component Q_{FF} which has contributions

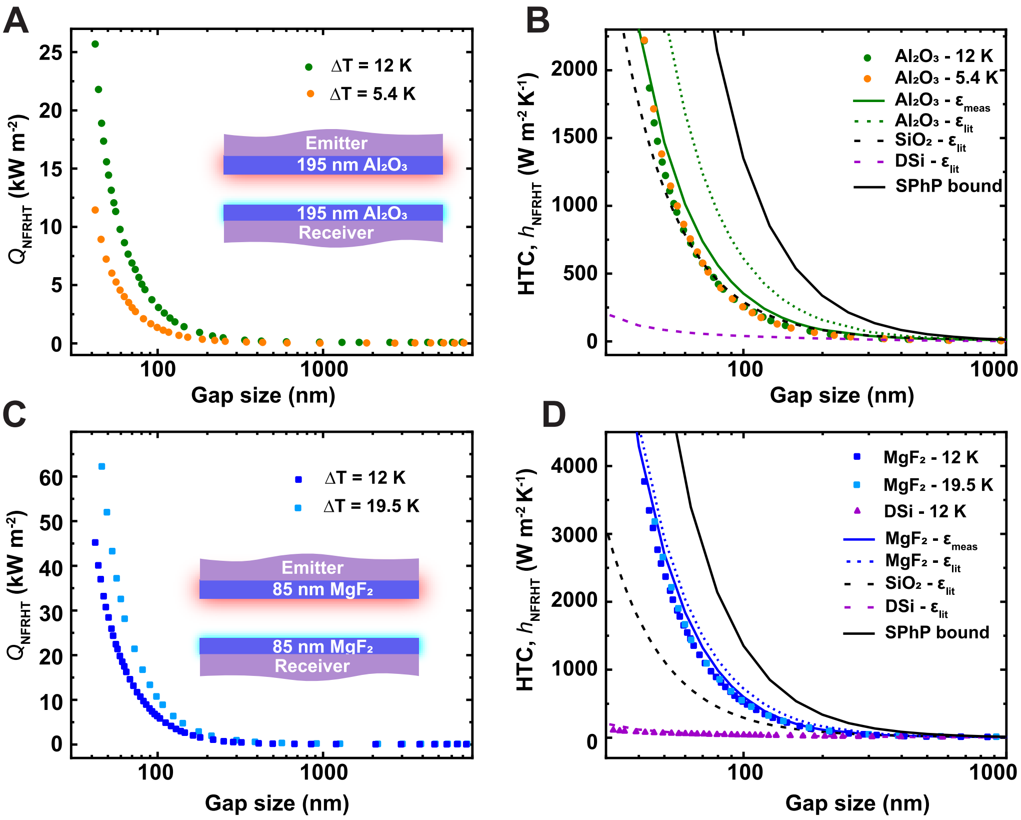

Figure 4. Experimental results of enhanced NFRHT for Al_2O_3 and MgF_2. (a) Radiative heat fluxes measured as a function of gap size, between Al_2O_3 plates and for two starting temperature differentials (green and orange circular markers). (b) Near-field thermal heat conductances extracted from (a), for gap sizes ranging from 1 μm to 50 nm. Theoretical NFRHT values calculated using literature values for the permittivities predict a slightly larger NFRHT but using our measured dielectric permittivities lead to close agreement. (c) Same as (a), but for MgF_2 (light and dark blue squares). (d) Same as (b), but for MgF_2-coated surfaces. Data for the NFRHT for silica (dashed black line), doped Si (dashed purple line), and the theoretical upper bound for SPhP materials (black dashed line) are also included for comparison. In agreement with our modeling, the experimentally observed values closely approach the HTC in SPhP materials.

from the "mesa" and the "rec" regions (the region on the emitter that is always in the far-field as shown in Figure 3B) of the emitter: $Q_{NFRHT} = Q_{NF} + Q_{FF}$. Based on this radiative heat flux, we then define a radiative HTC, normalized by the absolute temperature difference between the emitter and the receiver as $h_{NFRHT} = Q_{NFRHT}/(\Delta T_{ref} - \Delta T_{NF})$, where ΔT_{ref} is calculated as Q_{in}/G_{dev}.

Experiments start at a gap size of ~8 μm which is subsequently reduced until contact is established using a feedback-controlled piezoelectric actuator that displaces the receiver (Figure 3B). Mechanical contact between the devices is detected optically by focusing a laser (635 nm) on the backside of the emitter and collecting reflected light in a split photodiode. A small sinusoidal AC voltage at 3 kHz is applied to the piezo-actuator causing the receiver to oscillate at an amplitude of ~1.76 nm. A sudden change in the detected optical signal unambiguously signals the formation of a contact between the emitter and the receiver as the emitter begins to oscillate at this frequency. Figure 3C shows real-time data acquired before contact is made between the emitter and the receiver. As the gap size is reduced, the emitter temperature drops due to the increasing HTC between the emitter and the receiver. The temperature signal remains relatively constant between gap sizes of 8 μm and 500 nm, whereas at smaller gap sizes, large changes are observed that scale approximately[17] as $1/d^2$, as expected for NFRHT.

Results from our experiments using devices coated with MgF_2 or Al_2O_3 are shown in Figure 4. To perform these experiments, thin films of MgF_2 or Al_2O_3 were deposited on the emitter and receiver as described above (and in Supporting Information), with the emitters initially heated at large gap sizes such that ΔT_{ref} = 12 K. In addition, measurements are made at different ΔT_{ref} values of 5.4 K (Figures 4A,B) and 19 K (Figure 4C,D) to ensure repeatability of our results when the emitter is heated to different initial temperatures. The radiative heat fluxes as a function of gap size are shown in Figure 4A,C, down to ~45 nm gap sizes, immediately before contact, where Q_{NFRHT} exhibits a 500-fold enhancement over its far-field value, reaching 62 kW m^{-2} for MgF_2 and 38 kW m^{-2} for Al_2O_3 at a similar temperature difference of 12 K. The radiative HTCs, h_{NFRHT}, are shown in Figure 4B,D. The previously largest observed HTC at 50 nm gap sizes was 1075 W m^{-2} K^{-1}, for NFRHT between SiO_2 plates.[21,24] In part (b), we show measurements for Al_2O_3 of HTC values reaching ~1200 W m^{-2} K^{-1} at the same gap sizes, and in part (d) we show measurements for MgF_2 that reach ~2500 W m^{-2} K^{-1}. The latter measurement achieves 47% of the global SPhP bound (black solid lines) and is a new record at 50 nm gap sizes.

The HTCs that are extracted from the measured heat fluxes, as plotted in Figures 4B,D, follow nearly identical curves, as expected for HTCs, given the small difference in temperature. To confirm that the NF enhancement is due to the presence of the polar-dielectric films, we also performed control experiments between the emitter and receiver without a polar dielectric layer deposited on the Si surfaces (magenta markers). These silicon devices (DSi) were n-doped with phosphorus, 400 nm deep at a doping concentration of 2.7×10^{21} cm^{-3}. While the DSi-DSi measurements serve as control experiments for this study, they also are the first NFRHT measurements between doped silicon plates at gap sizes down to 25 nm.

Finally, we develop theoretical models of the expected heat fluxes and HTC (colored solid lines in Figure 4; see Supporting Information for spectral heat transfer and dispersion plots) that show close agreement with the experimental measurements. The total radiative conductance is calculated as the sum of the contributions from the "mesa" which is directly in the NF, and the recessed region "rec". The "mesa" structure is modeled as a 6-layer device (Figure 2B), while the "rec" region is modeled as a 4-layer structure. The receiver is modeled as a 2-layer structure with the thin dielectric on silicon substrate. The dielectric functions of materials (Si, SiO_2, doped Si), necessary for these calculations, were acquired from past work[45,46] (represented as $\varepsilon_{\mathrm{lit}}$ in Figure 4). However, the published optical data on MgF_2[45,47] and Al_2O_3[45,48,49] films vary widely due to different deposition conditions and sample preparation. Therefore, we directly measured the optical constants for MgF_2 and Al_2O_3 for free-space wavelengths 1.7−33 μm with a spectroscopic ellipsometer (see Supporting Information). The deposited MgF_2 shows significant inhomogeneous broadening of the SPhP resonance around 69 meV due to the amorphous nature of the films (see Supporting Information). The small discrepancies between the computed and experimental results can be attributed to differences in dielectric functions and small deviations from planarity and parallelism between the devices.

We note that our optimization of NFRHT phonon-polariton materials subject to the LST relation revealed an optimal material with a resonance frequency at 67 meV. This, in fact, is in line with past work[39] by some of us, where it was discovered that optimal materials for maximum NFRHT between bodies described by any causal susceptibilities should have a key characteristic property: Surface-wave resonances must occur at a smaller "near-field Wien frequency" of 67 meV or 19 μm free space wavelength (for operation at 300 K). This is in contrast to the predictions of Wien's law that, in the far-field, RHT attains a maximum at a frequency of ∼100−130 meV (300 K).[50] We note that, due to the narrow-band nature of NFRHT, the optimum frequency is red-shifted to 67 meV, which we term as the "near-field Wien frequency" at room temperature. Thus, our optimization for Drude−Lorentz permittivities in this work, validated by the experimental measurements when combined with our computational analysis of materials with Drude-like permittivities in a previous work,[39] reveal a universal framework for identifying materials with maximum NFRHT: Materials supporting strong resonances at "near-field Wien frequencies" can maximize NFRHT between two bodies.

In this work, we experimentally probed NFRHT at room temperature and demonstrated record near-field HTCs in MgF_2 and Al_2O_3 for gap sizes ranging from 1 μm to below 50 nm. We show that these materials support significantly larger NFRHT compared to those previously considered, such as SiO_2, because they support SPhP resonances close to the near-field Wien frequency. Strikingly, the near-field conductance of MgF_2 approaches within 47% of the theoretical upper bound for any SPhP resonance. Looking forward, we anticipate that new material platforms or architectures will be necessary for further enhancements of NFRHT. For example, plasmon-mediated NFRHT arising from free-electron response can yield further increases beyond SPhPs (due to broader resonances) but will require new doping schemes or novel 2D-material measurements. Alternatively, structured metasurfaces or Van der Waals heterostructures offer additional geometrical degrees of freedom; a combination of optimal materials and optimal structuring may lead to the ultimate limits of NFRHT.

■ ASSOCIATED CONTENT

Data Availability Statement

The data that support the findings of this study are available from the corresponding authors upon reasonable request.

Supporting Information

The Supporting Information is available free of charge at https://pubs.acs.org/doi/10.1021/acs.nanolett.2c04735.

Device fabrication and thin-film deposition, theoretical modeling and simulations, thermal characteristics of devices, X-ray diffraction measurements, measured dielectric functions of MgF_2 and Al_2O_3, discussion on the spectral nature of NFRHT, and theoretical optimization details (PDF)

■ AUTHOR INFORMATION

Corresponding Authors

Owen D. Miller − *Department of Applied Physics and Energy Sciences Institute, Yale University, New Haven, Connecticut 06511, United States;* orcid.org/0000-0003-2745-2392; Email: owen.miller@yale.edu

Pramod Reddy − *Department of Mechanical Engineering, University of Michigan, Ann Arbor, Michigan 48109, United States; Department of Materials Science, University of Michigan, Ann Arbor, Michigan 48109, United States;* orcid.org/0000-0002-7442-6931; Email: pramodr@umich.edu

Edgar Meyhofer − *Department of Mechanical Engineering, University of Michigan, Ann Arbor, Michigan 48109, United States;* orcid.org/0000-0001-5719-6030; Email: meyhofer@umich.edu

Authors

Rohith Mittapally − *Department of Mechanical Engineering, University of Michigan, Ann Arbor, Michigan 48109, United States;* Present Address: (R.M.) Department of Mechanical Engineering, Massachusetts Institute of Technology, Cambridge, Massachusetts 02139, United States; orcid.org/0000-0002-0784-1369

Ju Won Lim − *Department of Materials Science, University of Michigan, Ann Arbor, Michigan 48109, United States;* orcid.org/0000-0001-7021-3173

Lang Zhang − *Department of Applied Physics and Energy Sciences Institute, Yale University, New Haven, Connecticut 06511, United States;* orcid.org/0000-0001-7477-6715

Complete contact information is available at: https://pubs.acs.org/10.1021/acs.nanolett.2c04735

Author Contributions

O.M., P.R., and E.M. conceived the work. R.M. fabricated the devices, conducted the experiments, and analyzed the data.

R.M. and J.W.L. deposited the dielectric films and performed the characterization. L.Z. and R.M. performed the theoretical optimization and calculations. All authors contributed to writing the manuscript.

Notes

The authors declare no competing financial interest.

■ ACKNOWLEDGMENTS

P.R and E.M. acknowledge support from DOE-BES through a grant from the Scanning Probe Microscopy Division under Award No. DESC0004871 (Fabrication of Devices). O.M., P.R., and E.M. acknowledge support from the Army Research Office Award No. MURI W911NF-19-1-0279 (Experiments and Analysis).

■ REFERENCES

(1) Song, B.; Fiorino, A.; Meyhofer, E.; Reddy, P. Near-field radiative thermal transport: From theory to experiment. *AIP Adv.* **2015**, *5* (5), 053503.

(2) Cuevas, J. C.; Garcia-Vidal, F. J. Radiative Heat Transfer. *ACS Photonics* **2018**, *5* (10), 3896−3915.

(3) Biehs, S. A.; Messina, R.; Venkataram, P. S.; Rodriguez, A. W.; Cuevas, J. C.; Ben-Abdallah, P. Near-field radiative heat transfer in many-body systems. *Rev. Mod. Phys.* **2021**, *93* (2), 025009.

(4) Fiorino, A.; Zhu, L.; Thompson, D.; Mittapally, R.; Reddy, P.; Meyhofer, E. Nanogap near-field thermophotovoltaics. *Nat. Nanotechnol.* **2018**, *13* (9), 806−811.

(5) Bhatt, G. R.; Zhao, B.; Roberts, S.; Datta, I.; Mohanty, A.; Lin, T.; Hartmann, J. M.; St-Gelais, R.; Fan, S. H.; Lipson, M. Integrated near-field thermo-photovoltaics for heat recycling. *Nat. Commun.* **2020**, *11* (1), 2545.

(6) Lucchesi, C.; Cakiroglu, D.; Perez, J. P.; Taliercio, T.; Tournie, E.; Chapuis, P. O.; Vaillon, R. Near-Field Thermophotovoltaic Conversion with High Electrical Power Density and Cell Efficiency above 14%. *Nano Lett.* **2021**, *21* (11), 4524−4529.

(7) Mittapally, R.; Lee, B.; Zhu, L.; Reihani, A.; Lim, J. W.; Fan, D.; Forrest, S. R.; Reddy, P.; Meyhofer, E. Near-field thermophotovoltaics for efficient heat to electricity conversion at high power density. *Nat. Commun.* **2021**, *12* (1), 4364.

(8) Zhu, L.; Fiorino, A.; Thompson, D.; Mittapally, R.; Meyhofer, E.; Reddy, P. Near-field photonic cooling through control of the chemical potential of photons. *Nature* **2019**, *566* (7743), 239−244.

(9) Chen, K. F.; Santhanam, P.; Sandhu, S.; Zhu, L. X.; Fan, S. H. Heat-flux control and solid-state cooling by regulating chemical potential of photons in near-field electromagnetic heat transfer. *Phys. Rev. B* **2015**, *91* (13), 134301.

(10) Fiorino, A.; Thompson, D.; Zhu, L. X.; Mittapally, R.; Biehs, S. A.; Bezencenet, O.; El-Bondry, N.; Bansropun, S.; Ben-Abdallah, P.; Meyhofer, E.; et al. A Thermal Diode Based on Nanoscale Thermal Radiation. *ACS Nano* **2018**, *12* (6), 5774−5779.

(11) Ben-Abdallah, P.; Biehs, S. A. Contactless heat flux control with photonic devices. *AIP Adv.* **2015**, *5* (5), 053502.

(12) Otey, C. R.; Lau, W. T.; Fan, S. H. Thermal Rectification through Vacuum. *Phys. Rev. Lett.* **2010**, *104* (15), 154301.

(13) Challener, W. A.; Peng, C. B.; Itagi, A. V.; Karns, D.; Peng, W.; Peng, Y. G.; Yang, X. M.; Zhu, X. B.; Gokemeijer, N. J.; Hsia, Y. T.; et al. Heat-assisted magnetic recording by a near-field transducer with efficient optical energy transfer. *Nat. Photonics* **2009**, *3* (5), 220−224.

(14) Rytov, S. M. In *Theory of electric fluctuations and thermal radiation*; Air Force Cambrige Research Center: Bedford, MA, 1953.

(15) Rytov, S. M.; Kravtsov, Y. A.; Tatarskii, V. I. In *Principles of statistical radiophysics*; Springer-Verlag: Berlin, Heidelberg, 1989.

(16) Polder, D.; Vanhove, M. Theory of Radiative Heat Transfer between Closely Spaced Bodies. *Phys. Rev. B* **1971**, *4* (10), 3303−3314.

(17) Joulain, K.; Mulet, J. P.; Marquier, F.; Carminati, R.; Greffet, J. J. Surface electromagnetic waves thermally excited: Radiative heat transfer, coherence properties and Casimir forces revisited in the near field. *Surf. Sci. Rep.* **2005**, *57* (3−4), 59−112.

(18) Otey, C. R.; Zhu, L. X.; Sandhu, S.; Fan, S. H. Fluctuational electrodynamics calculations of near-field heat transfer in non-planar geometries: A brief overview. *J. Quant. Spectrosc. Ra.* **2014**, *132*, 3−11.

(19) Song, B.; Ganjeh, Y.; Sadat, S.; Thompson, D.; Fiorino, A.; Fernandez-Hurtado, V.; Feist, J.; Garcia-Vidal, F. J.; Cuevas, J. C.; Reddy, P.; et al. Enhancement of near-field radiative heat transfer using polar dielectric thin films. *Nat. Nanotechnol.* **2015**, *10* (3), 253−258.

(20) Song, B.; Thompson, D.; Fiorino, A.; Ganjeh, Y.; Reddy, P.; Meyhofer, E. Radiative heat conductances between dielectric and metallic parallel plates with nanoscale gaps. *Nat. Nanotechnol.* **2016**, *11* (6), 509−514.

(21) Fiorino, A.; Thompson, D.; Zhu, L. X.; Song, B.; Reddy, P.; Meyhofer, E. Giant Enhancement in Radiative Heat Transfer in Sub-30 nm Gaps of Plane Parallel Surfaces. *Nano Lett.* **2018**, *18* (6), 3711−3715.

(22) Lim, M.; Song, J.; Lee, S. S.; Lee, B. J. Tailoring near-field thermal radiation between metallo-dielectric multilayers using coupled surface plasmon polaritons. *Nat. Commun.* **2018**, *9*, 4302.

(23) DeSutter, J.; Tang, L.; Francoeur, M. A near-field radiative heat transfer device. *Nat. Nanotechnol.* **2019**, *14* (8), 751−755.

(24) Salihoglu, H.; Nam, W.; Traverso, L.; Segovia, M.; Venuthurumilli, P. K.; Liu, W.; Wei, Y.; Li, W. J.; Xu, X. F. Near-Field Thermal Radiation between Two Plates with Sub-10 nm Vacuum Separation. *Nano Lett.* **2020**, *20* (8), 6091−6096.

(25) Tang, L.; DeSutter, J.; Francoeur, M. Near-Field Radiative Heat Transfer between Dissimilar Materials Mediated by Coupled Surface Phonon- and Plasmon-Polaritons. *ACS Photonics* **2020**, *7* (5), 1304−1311.

(26) Ottens, R. S.; Quetschke, V.; Wise, S.; Alemi, A. A.; Lundock, R.; Mueller, G.; Reitze, D. H.; Tanner, D. B.; Whiting, B. F. Near-Field Radiative Heat Transfer between Macroscopic Planar Surfaces. *Phys. Rev. Lett.* **2011**, *107* (1), 014301.

(27) Wang, X. J.; Basu, S.; Zhang, Z. M. Parametric optimization of dielectric functions for maximizing nanoscale radiative transfer. *J. Phys. D Appl. Phys.* **2009**, *42* (24), 245403.

(28) Nefzaoui, E.; Ezzahri, Y.; Drevillon, J.; Joulain, K. Maximal near-field radiative heat transfer between two plates. *Eur. Phys. J-Appl. Phys.* **2013**, *63* (3), 30902.

(29) Mulet, J. P.; Joulain, K.; Carminati, R.; Greffet, J. J. Enhanced radiative heat transfer at nanometric distances. *Microscale Therm. Eng.* **2002**, *6* (3), 209−222.

(30) Biehs, S. A.; Tschikin, M.; Ben-Abdallah, P. Hyperbolic Metamaterials as an Analog of a Blackbody in the Near Field. *Phys. Rev. Lett.* **2012**, *109* (10), 104301.

(31) Liu, X. L.; Zhang, R. Z.; Zhang, Z. M. Near-field radiative heat transfer with doped-silicon nanostructured metamaterials. *Int. J. Heat Mass Trans.* **2014**, *73*, 389−398.

(32) Fernandez-Hurtado, V.; Garcia-Vidal, F. J.; Fan, S. H.; Cuevas, J. C. Enhancing Near-Field Radiative Heat Transfer with Si-based Metasurfaces. *Phys. Rev. Lett.* **2017**, *118* (20), 203901.

(33) Liu, X. L.; Zhang, Z. M. Near-Field Thermal Radiation between Metasurfaces. *ACS Photonics* **2015**, *2* (9), 1320−1326.

(34) Ben-Abdallah, P.; Joulain, K.; Drevillon, J.; Domingues, G. Near-field heat transfer mediated by surface wave hybridization between two films. *J. Appl. Phys.* **2009**, *106* (4), 044306.

(35) Iizuka, H.; Fan, S. Significant Enhancement of Near-Field Electromagnetic Heat Transfer in a Multilayer Structure through Multiple Surface-States Coupling. *Phys. Rev. Lett.* **2018**, *120* (6), 063901.

(36) Francoeur, M.; Menguc, M. P.; Vaillon, R. Near-field radiative heat transfer enhancement via surface phonon polaritons coupling in thin films. *Appl. Phys. Lett.* **2008**, *93* (4), 043109.

(37) Miller, O. D.; Johnson, S. G.; Rodriguez, A. W. Shape-Independent Limits to Near-Field Radiative Heat Transfer. *Phys. Rev. Lett.* **2015**, *115* (20), 204302.

(38) Venkataram, P. S.; Molesky, S.; Jin, W. L.; Rodriguez, A. W. Fundamental Limits to Radiative Heat Transfer: The Limited Role of Nanostructuring in the Near-Field. *Phys. Rev. Lett.* **2020**, *124* (1), 013904.

(39) Zhang, L.; Miller, O. D. Optimal Materials for Maximum Large-Area Near-Field Radiative Heat Transfer. *ACS Photonics* **2020**, *7* (11), 3116−3129.

(40) Shim, H.; Monticone, F.; Miller, O. D. Fundamental limits to the refractive index of transparent optical materials. *Adv. Mater.* **2021**, *33*, 2103946.

(41) Lyddane, R. H.; Sachs, R. G.; Teller, E. On the polar vibrations of alkali halides. *Phys. Rev.* **1941**, *59* (8), 673−676.

(42) Barker, A. S. Long-Wavelength Soft Modes, Central Peaks, and Lyddane-Sachs-Teller Relation. *Phys. Rev. B* **1975**, *12* (10), 4071−4084.

(43) Ganjeh, Y.; Song, B.; Pagadala, K.; Kim, K.; Sadat, S.; Jeong, W.; Kurabayashi, K.; Meyhofer, E.; Reddy, P. A platform to parallelize planar surfaces and control their spatial separation with nanometer resolution. *Rev. Sci. Instrum.* **2012**, *83* (10), 105101.

(44) Sadat, S.; Meyhofer, E.; Reddy, P. High resolution resistive thermometry for micro/nanoscale measurements. *Rev. Sci. Instrum.* **2012**, *83* (8), 084902.

(45) Palik, E. D. In *Handbook of optical constants of solids*; Academic Press: San Diego, 1998.

(46) Basu, S.; Lee, B. J.; Zhang, Z. M. Near-Field Radiation Calculated With an Improved Dielectric Function Model for Doped Silicon. *J. Heat Trans-T. ASME* **2010**, *132* (2), 023302.

(47) Franta, D.; Necas, D.; Giglia, A.; Franta, P.; Ohlidal, I. Universal dispersion model for characterization of optical thin films over wide spectral range: Application to magnesium fluoride. *Appl. Surf. Sci.* **2017**, *421*, 424−429.

(48) Kischkat, J.; Peters, S.; Gruska, B.; Semtsiv, M.; Chashnikova, M.; Klinkmuller, M.; Fedosenko, O.; Machulik, S.; Aleksandrova, A.; Monastyrskyi, G.; Flores, Y.; Masselink, W. T. Mid-infrared optical properties of thin films of aluminum oxide, titanium dioxide, silicon dioxide, aluminum nitride, and silicon nitride. *Appl. Opt.* **2012**, *51*, 6789−6798.

(49) Shi, S. Z.; Qian, S.; Hou, X. J.; Mu, J. L.; He, J.; Chou, X. J. Structural and optical properties of amorphous Al_2O_3 thin film deposited by atomic layer deposition. *Adv. Cond. Matter Phys.* **2018**, *2018*, 7598978.

(50) Heald, M. A. Where is the ″Wien peak″? *Am. J. Phys.* **2003**, *71* (12), 1322−1323.

Supporting Information

Probing the Limits to Near-Field Heat Transfer Enhancements in Phonon-Polaritonic Materials

Rohith Mittapally[1,‡], *Ju Won Lim*[2], *Lang Zhang*[3], *Owen D. Miller*[3 *], *Pramod Reddy*[1,2 *], *Edgar Meyhofer*[1 *]

[1]Department of Mechanical Engineering, University of Michigan, Ann Arbor, MI 48109, USA

[2]Department of Materials Science, University of Michigan, Ann Arbor, MI 48109, USA.

[3]Department of Applied Physics and Energy Sciences Institute, Yale University, New Haven, CT 06511, USA.

1. Device fabrication and deposition of dielectric films

The micro-fabrication procedure for the emitter devices is shown Figure S1 and is related to previous work (4,8,10). Briefly, we start (step 1) with a double silicon-on-insulator (SOI) wafer with a 15 µm-thick top crystalline-Si device layer, separated from the 40 µm-thick crystalline-Si middle layer via a 1 µm-thick silicon dioxide layer. Another 1 µm-thick silicon dioxide layer separates these two layers from a 500 µm-thick Si handle layer. A ~400 nm-thick n-doped ($2.7 \times 10^{20}\ cm^{-3}$) layer is grown on this wafer by phosphorous diffusion at 975º C for 12 minutes (step 2). This wafer is then lithographically patterned and etched using a reactive ion etching (RIE) tool to form the 15 µm-thick mesa structure (step 3). Subsequently, two layers of 30 nm and 100 nm-thick platinum were deposited by lift-off techniques, forming the thermometer, heater and electrical contacts (step 4). Next, the wafer is patterned using a thick photoresist (AZ 9260) to protect the mesa, and to define the structure of the beams and the island. The two oxide layers and the 40 µm-thick middle Si layers are successively etched in a RIE process (step 5). An appropriately sized window is made on the backside of the wafer and the 500 µm-thick Si handle layer is etched in an RIE process, stopping at the backside of the emitter. The devices are then cleaned in acetone, IPA and piranha to strip the photoresist and other contaminants introduced during the processing. This (step 6) completes the release of the emitter devices.

Finally (step 7), we deposit thin films of the two dielectrics described in this work. MgF_2 is deposited using evaporation technique in an SJ-20 e-beam evaporator. The deposition rate is characterized by measuring the deposited thickness in Nanospec 6100, a non-contact spectroscopic reflectometry technique. The 194 nm-thick amorphous layer of Al_2O_3 is deposited in a thermal-assisted atomic layer deposition technique (Veeco Fiji atomic layer deposition tool). Trimethylaluminum (TMA - $Al(CH_3)_3$) and H_2O were used as the precursor of metallic aluminum and oxygen ions, and the deposition was performed at a temperature of 200° C. The optical constants of the two dielectric films were measured by J.A. Woollam Co. Ellipsometry solutions.

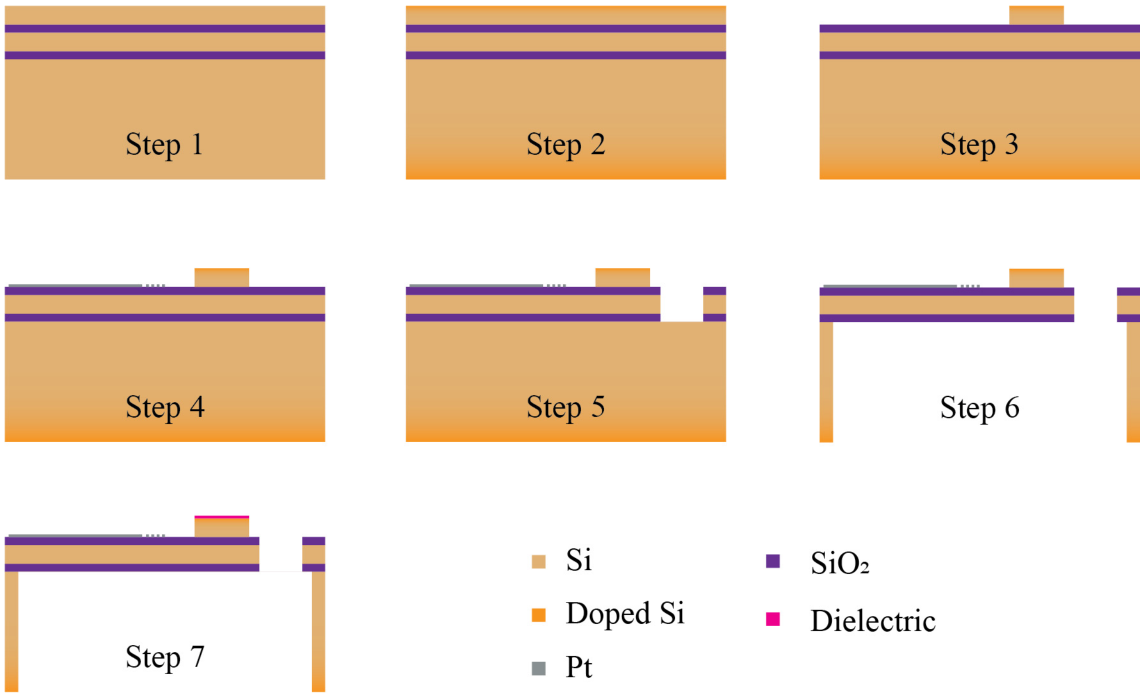

Figure S1. *Steps involved in fabrication of the emitter device.*

2. Theoretical Modeling

We treat the two bodies as homogenous, isothermal and semi-infinite objects with multilayered structures. The different materials present in each body are represented schematically in Figure 1c of the main manuscript. The net radiative heat transfer $q(T_1, T_2, d)$ is then calculated as:

$$q(T_1,T_2,d)=\int_0^\infty \frac{d\omega}{4\pi^2}\left[\Theta(\omega,T_1)-\Theta(\omega,T_2)\right]\int_0^\infty dkk\left[\tau_s(\omega,k)+\tau_p(\omega,k)\right],$$

where T_1 and T_2 are the temperatures of the emitter and the receiver, d is the gap-size, ω is the angular frequency of electromagnetic modes, k is the component of the wave-vector parallel to the interface, $\Theta(\omega, T_i) = \hbar\omega/\exp(\hbar\omega/(k_B T_i - 1))$ is the mean-energy of a Planck oscillator and τ_s and τ_p are the transmission probabilities of the s-polarized and the p-polarized modes, described by the following expressions

$$\tau^{12}_{\alpha=s,p}(\omega,k)=\begin{cases}\dfrac{(1-|R^1_\alpha|^2)(1-|R^2_\alpha|^2)}{|D_\alpha|^2}, \text{ if } k<\omega/c, \text{ propagating waves}\\ \dfrac{4\,\mathrm{Im}\left(R^1_\alpha\right)\mathrm{Im}\left(R^2_\alpha\right)e^{-2\,\mathrm{Im}(\gamma_0)d}}{|D_\alpha|^2}, \text{ if } k>\omega/c, \text{ evanascent waves}\end{cases}$$

Here, R_α^i is the Fresnel reflection-coefficient of the multi-layer structure where the super-script i refers to the body 1 or body 2. These coefficients are calculated for each body, starting from the vacuum side (referred to as medium ‘0’), based on standard theory of layered media (1). The Fresnel reflection coefficient at any interface between media i and j for the s-polarization is $r_s^{i,j} = (\gamma_i-\gamma_j)/(\gamma_i+\gamma_j)$ and for the p-polarization is given by $r_p^{i,j} = (\varepsilon_j\gamma_i-\varepsilon_i\gamma_j)/(\varepsilon_j\gamma_i+\varepsilon_i\gamma_j)$, where $\gamma_i = \sqrt{\varepsilon_i(\omega)\,\omega^2/c^2-k^2}$ is the component of the wave-vector perpendicular to the interface; $\varepsilon_i(\omega)$ is the frequency-dependent dielectric permittivity of the i^{th} medium, c is the speed of light and $D_\alpha = 1-R_\alpha^1\,R_\alpha^2 e^{2i\gamma_0 d}$. To account for the anisotropic dielectric permittivity of MgF$_2$ (birefringence: ordinary, ε_o and extraordinary, ε_e components of the dielectric permittivity, ε_{lit}), the expressions are modified to $\gamma_s = \sqrt{\varepsilon_o(\omega)\,\omega^2/c^2-k^2}$ and $\gamma_p = \sqrt{\varepsilon_o(\omega)\,\omega^2/c^2-\varepsilon_o(\omega)k^2/\varepsilon_e(\omega)}$ and the ordinary component used in the calculation of reflection coefficients (2). Finally, the radiative heat transfer coefficient $h(T$, d) can be either calculated as $q(T_1,T_2,d)/(T_1-T_2)$ or

$$h(T,d)\equiv\lim_{(T_1-T_2)\to 0}\left|\frac{q(T_1,T_2,d)}{T_1-T_2}\right|=\int_0^\infty\frac{d\omega}{4\pi^2}\frac{\partial\Theta(\omega,T)}{\partial T}\int_0^\infty dkk\left[\tau_s(\omega,k)+\tau_p(\omega,k)\right].$$

In order to compare our experimental results with theoretical expectation, we consider our device structure to consist of two distinct regions ‘mesa’ and ‘rec’ (shown in Figures 2B and 3B of main manuscript). At each gap size, the contributions from mesa and rec were calculated using the framework described above. The total radiative heat transfer coefficient is then defined as the sum of the contributions from mesa and rec.

3. Thermal characterization of the emitter devices

In order to characterize the thermal properties of our suspended emitters, we employed a half-Wheatstone bridge as shown in Figure S2a. A known current I_{AC} is passed through the serpentine resistor ($R_{serpentine}$) and a potentiometer whose resistance ($R_{matching}$) is set to match that of the platinum resistor. The voltages across the platinum resistor and the matching resistor are fed to two instrumentation amplifiers (AD524) with a unity gain. The outputs from these first-stage amplifiers are then fed to the second-stage amplifier with a unity gain, thus obtaining a good common-mode rejection. The signal at this point is fed to a lock-in amplifier (SR830) and the voltage at the relevant frequency and harmonic are monitored during the experiment.

The temperature changes associated with the near-field radiative heat flux are measured by monitoring the associated resistance change (ΔR) of the serpentine platinum resistor on the emitter device. An AC current I_{AC} = 70 μA at a frequency of 497 Hz is passed through the circuit shown in Figure S2a. The voltage change ΔV_{AC} at this frequency is then measured using an SR830 lock-in amplifier. The temperature change is calculated as

$$\Delta T_{AC} = \frac{\Delta V_{AC}}{I_{AC} R_0 \alpha}$$

where R_0 is the resistance of the platinum resistor at room temperature (300 K) and $\alpha = 1.86 \pm 0.03 \times 10^{-3}$ K^{-1} is the temperature coefficient of resistance (TCR).

Platinum thermometry

The TCR of the thin film platinum resistor was characterized in an independent measurement, where the fabricated device was mounted on the cold finger of a Janis ST-100 cryostat, whose temperature was controlled using a Lakeshore 335 temperature controller. The resistance of the device was measured by passing a current of 1 μA at a frequency of 1 kHz using a Keithley 6221 current source, while the amplitude of the associated sinusoidal voltage signal was measured using an SR830 lock-in amplifier. The measured resistance changes as a function of the temperature from 298 K to ~311 K is plotted in Figure S2b, which indicates good linearity. The slope (dR/dT) obtained by fitting a linear equation on this data is 7.29 ± 0.11 Ω K^{-1}. Thus, the TCR or α is measured to be $1.86 \pm 0.03 \times 10^{-3}$ K^{-1}.

Frequency response of the emitter

The frequency response of our emitter is characterized by measuring modulated temperature changes at second harmonic (ΔT_{2f}) associated with heat dissipation (Q_{2f}). A sinusoidal current with an amplitude of I_{AC} = 300 µA is passed through the circuit, while the frequency, f is varied from 0.2 Hz to 600 Hz. This causes a heat dissipation in the emitter with a DC component and an AC component at $2f$, $Q_{2f} = I_{AC}{}^2 R/2$, where R is the resistance of the platinum resistor. This causes the emitter's temperature to fluctuate at $2f$, ΔT_{2f}. Since, we measure the resistance change associated with this temperature modulation using sinusoidal current at f, amplitude of the sinusoidal voltage is measured at third harmonic, ΔV_{3f}. The temperature change is then related to the sinusoidal voltage signal as

$$\Delta T_{2f} = \frac{2\Delta V_{3f}}{I_{AC} R_0 \alpha}$$

This modulated temperature change as a function of the frequency applied, f is plotted in Figure S2c. A full thermal response is achieved at frequencies below ~5 Hz, after which the signal starts to roll-off. From this curve, we estimate the time constant of our device to be 65 ms or a thermal cut-off frequency of 15 Hz.

Thermal Conductance of the beam

The thermal conductance of the device (G_{dev}) is calculated in a 3f-measurement scheme, where a sinusoidal current at a fixed frequency of 1 Hz – chosen for a full thermal response of the device – is passed through the platinum resistor and the amplitude is varied from 300 µA to 1.2 mA. This results in a temperature modulation at 2 Hz, which is calculated as described previously. The variation of $Q_{2f} = I_{AC}{}^2 R/2$ as a function of the temperature change ΔT_{2f} is plotted in Figure S2d. A clear linear relationship is observed in this temperature range, where the slope of the line revealed the thermal conductance of the emitter to be 261 ± 1.8 µW K^{-1}.

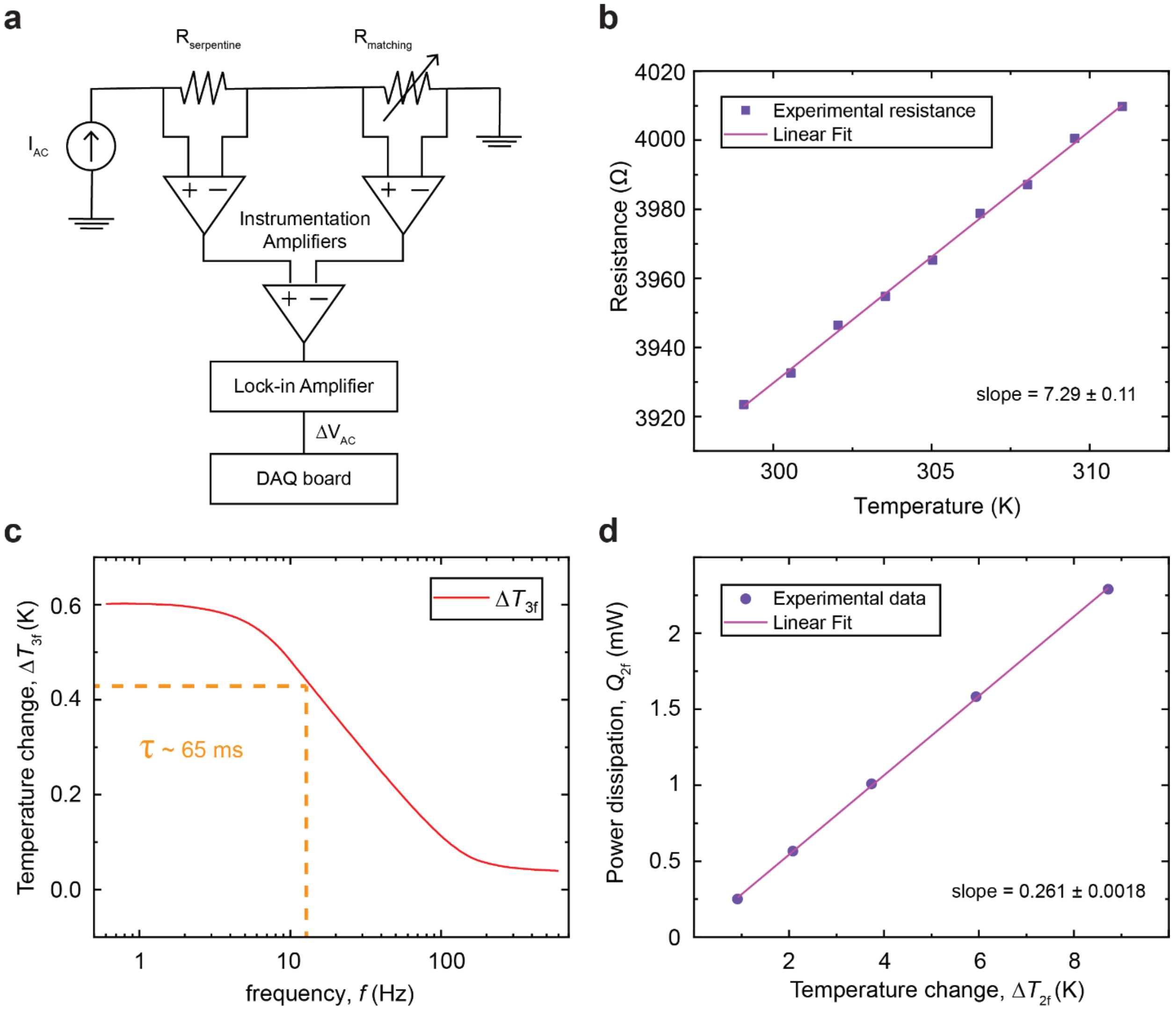

Figure S2. *Thermal characterization of the emitter device. (a) The electronic circuit employed to measure the temperature change by monitoring the associated resistance change.* $R_{serpentine}$ *and* $R_{matching}$ *are the resistances of the platinum resistor and a potentiometer. Two stages of instrumentation amplifiers aid in common-mode rejection. A lock-in amplifier detects the modulated signal which is then collected in a DAQ board. (b) The resistance of the platinum resistor (*$R_{serpentine}$*) as a function of its temperature. (c) The detected temperature change as a function of the frequency of the sinusoidal current passing through the platinum resistor. The frequency response indicates that the time constant of our device is ~65 ms. (d) The modulated power dissipation,* $Q_{2\omega}$ *as a function of the detected temperature change at 2f. The slope from the linear fit indicates that the thermal conductance of this device is 261 µW/K.*

4. Micro-structure characterization of the dielectric films

In order to understand the micro-structure of the deposited thin films and determine the cause for broadening observed in the measured dielectric functions, we have performed X-Ray diffraction measurements on silicon samples coated with MgF_2 and Al_2O_3 using a Rigaku Miniflex 600 X-Ray Diffractometer. A Cu K-α radiation in a 2θ range of 10–90° (current: 15 mA, voltage: 40 kV) was used as the source. A bare silicon sample was used as a reference and XRD patterns were quantitatively analyzed using an integrated X-ray diffraction software (PDXL). Supplementary Figure S3 shows the XRD pattern of the bare Si substrate, MgF_2 and Al_2O_3 coated Si substrates. The Si substrate exhibits two distinct peaks at 69.0º and 29.0º, corresponding to its crystal axes. The XRD peaks of MgF_2 films are almost identical with a bare Si XRD and no additional peaks are observed, implying that the deposited layer is entirely amorphous as previously observed in room-temperature deposition of MgF_2 films by evaporation (3,4). Likewise, the XRD peaks of Al_2O_3 film were mostly identical with bare Si, except the two additional peaks at 33.3º and 65.0º~70.0º. The broad peaks may indicate a mix of crystalline and amorphous phases as typically observed in ALD grown films (5). Especially, broad range peak at 65.0º~70.0º is a clear indication of α-alumina formed in the ALD process (6). From these XRD measurements, we conclude that two films deposited (MgF_2, Al_2O_3) are mostly amorphous.

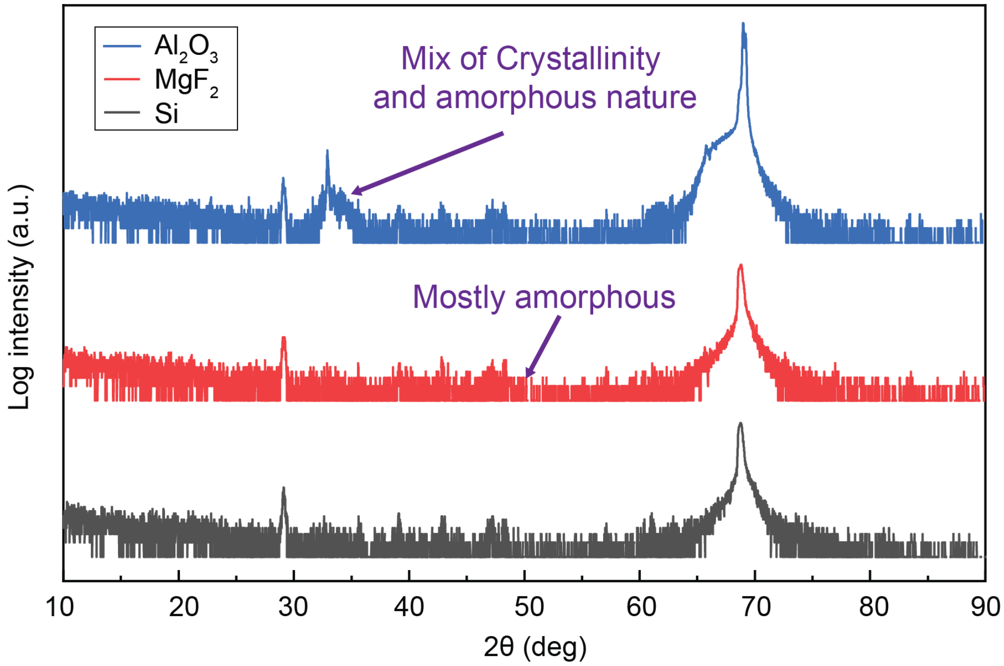

Figure S3. *X-ray diffraction measurements on bare Si and Si samples coated with 85 nm-thick* MgF_2 *and 194 nm-thick* Al_2O_3*.*

5. Dielectric films approach bulk case below gaps of 100 nm

In order to understand the effect of film thickness on the radiative heat transfer properties, we compare the theoretical h_{NFRHT} for each material in its bulk form and when deposited as a film on bulk Si. The results from these calculations are plotted in Figure S4c for different thicknesses of MgF_2, Al_2O_3 and SiO_2. Clearly, below a gap size of 100 nm, all the materials approach a trend, like that of the bulk counterparts and a significant deviation is observed for large gap sizes. When the gap size is comparable to or smaller than the thickness of the dielectric films, the penetration depth of the SPhP modes contributing to NFRHT becomes comparable to the gap size (7-9). Thus, at gap sizes smaller than the thickness of the films, the NFRHT between thin films approaches that of the bulk case, as seen in Figure S4c.

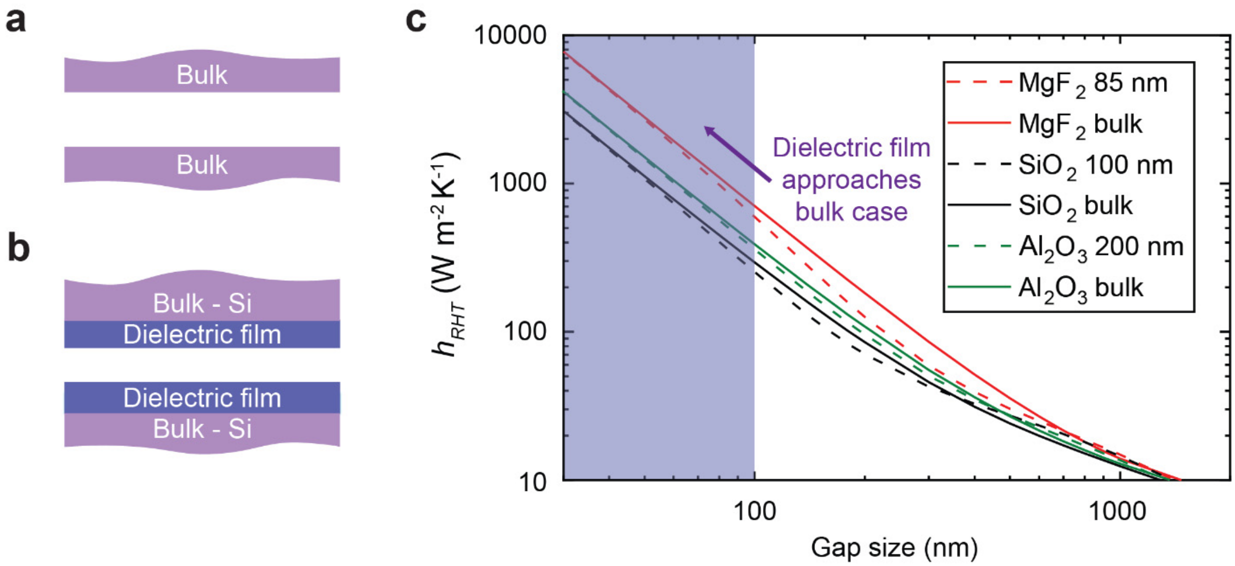

Figure S4. *NFRHT between bulk and thin-film materials. (a) Schematic of two semi-infinite plates depicting the bulk case for the dielectric films. (b) Schematic of the multi-layer structure with each object consisting of a dielectric film on a semi-infinite Si sample. (c) The calculated radiative heat transfer conductance as a function of gap size for different thin films and the corresponding bulk counterparts. Solid lines correspond to results for the bulk cases and dashed lines correspond to results for the thin-film cases.*

6. Dielectric function measurement

The optical constants *n* & *k* for the dielectric films coated on a silicon substrate were measured using an infrared ellipsometry technique in the wavelength range of 1.7 - 33 µm using an IR-VASE Mark II ellipsometer. The ellipsometry parameters, ψ and Δ at two incident angles of 55º and 65º were measured for MgF_2- and Al_2O_3-coated Si samples along with a bare Si sample for reference. A model satisfying the Kramers-Kronig relationship was then used to determine the thickness, refractive index and extinction coefficient as a function of the wavelength of the incident light. The parameters in the model were iteratively varied to find a good fit between experiments and theoretical calculations. The optical constants obtained in this method are shown in Figure S5. We use these measured dielectric functions in the theoretical framework described before, to calculate h_{NFRHT} as a function of gap size, for MgF_2 and Al_2O_3. All other dielectric functions of different materials discussed in this work were obtained from Ref. (10).

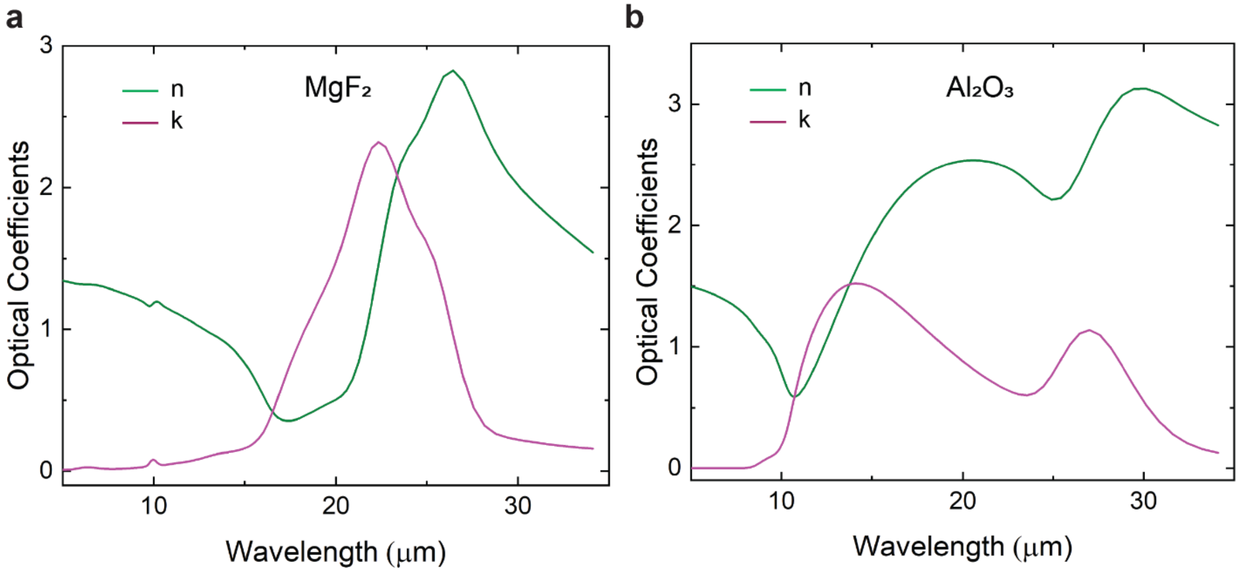

Figure S5. *Measured optical constants of the dielectric films, n and k for (a) MgF_2 coated sample and (b) Al_2O_3 coated sample.*

7. Spectral characteristics of NFRHT

To gain further insights into the mechanism for this enhancement, we plot the spectral radiative flux of our system for three gap sizes of 50 nm, 100 nm and 1000 nm in Figures S6a, c. A narrow-band NF enhancement is observed as the gap size is reduced from 1000 nm to 50 nm (solid lines calculated using measured dielectric function), due to the contribution from SPhP resonance in Al_2O_3 (Figure S6a) and MgF_2 (Figure S6c). A clear distinction between the width of the peaks can be noticed when compared with the calculations using dielectric functions based on crystalline MgF_2 (dashed lines) due to the amorphous nature of our films. In fact, the measured dielectric function showed significant inhomogenous broadening of the SPhP resonance around 67 meV. This is further supported by XRD characterization of the films which did not reveal any peaks other than that of the underlying silicon substrate, indicating the amorphous nature of the films. Due to the inherent broadband nature of RHT, such broadening of the resonances does not significantly affect h_{NFRHT}, as substantiated by the good match with our experimental data. More importantly, the SPhP resonance at 67 meV as opposed to that of 144 meV for the silica case, results in a 2.5-fold enhanced NFRHT. In Figures S6b, d, we also plot the transmission probabilities for the p-polarized modes, as a function of frequency (ω) and parallel wavevector (k) at a gap size of 50 nm. Q_{NFRHT} is dominated by the TM modes around ω = 67 meV with contributions ($\tau_p = 1$, shown in yellow band) from very large wavevectors (Figure S6d).

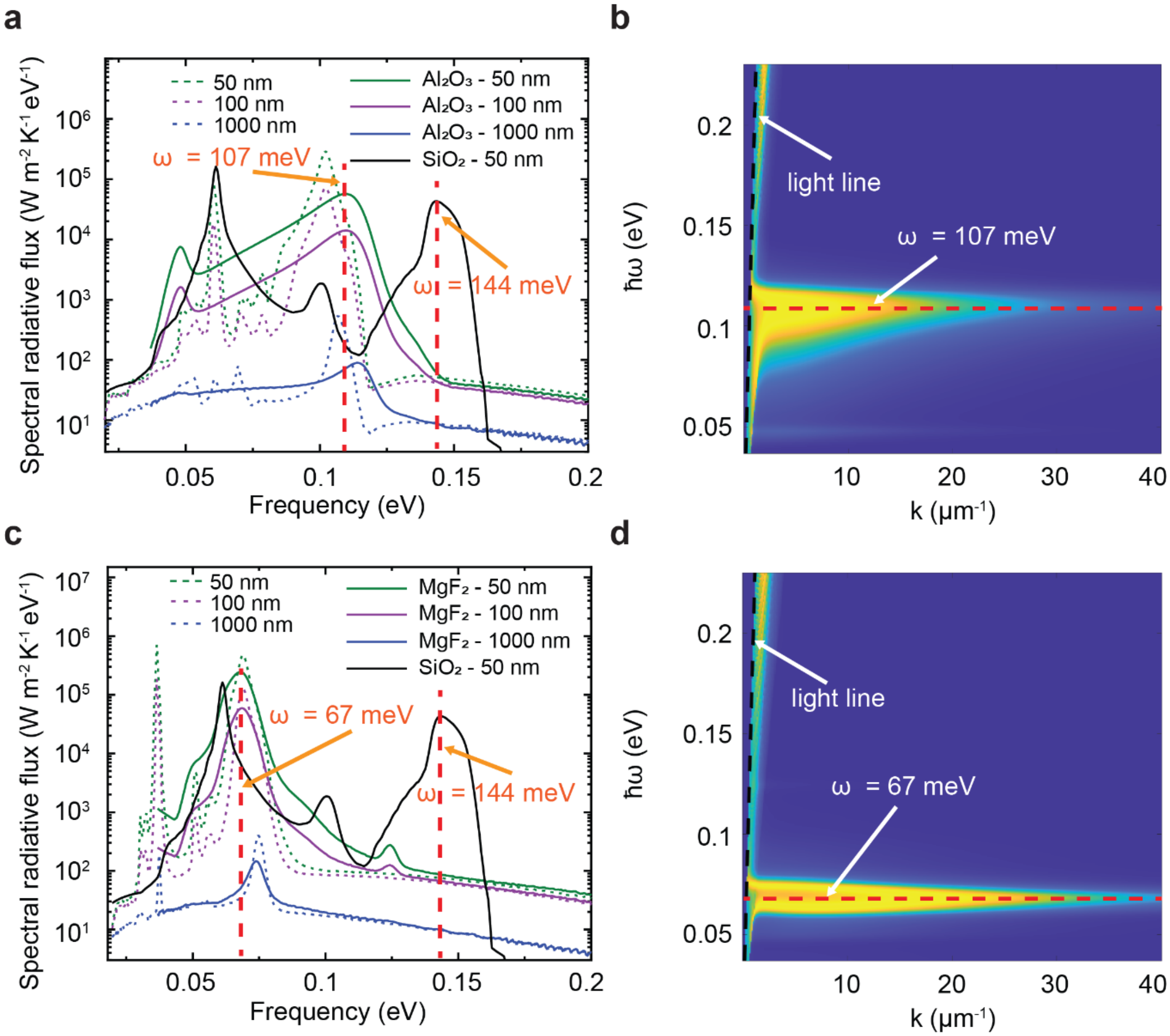

Figure S6. *Spectral characteristics of NFRHT. (a) Theoretical calculation of spectral radiative heat flux between the devices coated with Al_2O_3 in the frequency range of 0.02 - 0.2 eV for gap sizes of 50, 100 and 1000 nm. Solid lines represent the calculations based on the measured dielectric function while the dashed lines represent calculations based on dielectric function data from past measurements on crystalline Al_2O_3. The black solid line is the spectral heat flux for SiO_2 at a gap size of 50 nm. (b) The transmission probability of TM modes at a gap size of 50 nm, plotted as a function of frequency and parallel wavevector for Al_2O_3. The black dashed line indicates the light line. (c) same as (a) but for MgF_2. (d) same as (b) but for MgF_2.*

8. The Lyddane-Sachs-Teller (LST) relation in SPhP materials

What differentiates an SPhP material from free-electron-based polaritonic materials? Intuitively, we know that SPhP materials support narrow-band Drude-Lorentz-like permittivities, in constrast to the broad Drude-like response of free-electron-based SPP materials. As discussed in the main text, a key distinguishing feature related to the lineshapes noted above is that there is typically a ratio of the frequencies of the longitudinal optical phonon mode to the transverse optical phonon mode, ω_{LO}/ω_{TO}, that phonon-polaritonic materials do not surpass. These ratios play a central role in the Lyddane-Sachs-Teller (LST) relation (11,12): $(\omega_{LO}/\omega_{TO})^2 = \varepsilon_{st}/\varepsilon_\infty$, where ε_{st} and ε_∞ are the phonon-mode contributions to the static and high-frequency permittivities, and which also have similar values for any phonon. This constraint on ω_{LO}/ω_{TO} for phonon-polaritonic materials originates from compounded effects of the masses of atoms and the crystal structures of materials. An empirical upper limit of this ratio is 2 for common optical materials. The table and figure show specific optical phonon mode frequencies of some materials (10, 14-16).

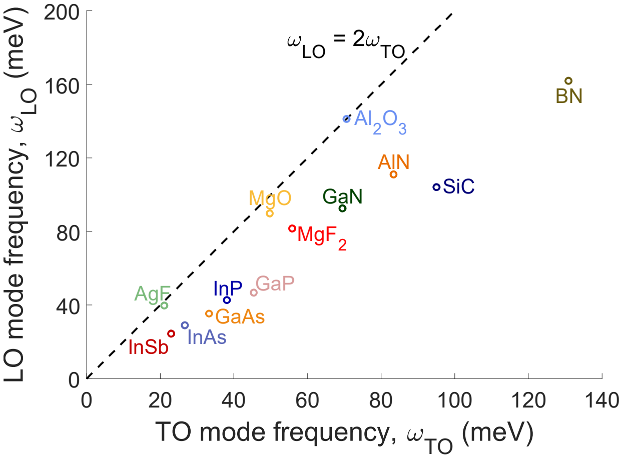

Figure S7. *Relationship between the LO and TO mode frequencies of common materials that support phonon-polaritons.*

	ω_{LO}(meV)	ω_{TO}(meV)	ω_{LO}/ω_{TO}	$\varepsilon_{st}/\varepsilon_{\infty}$
AgF	39.7	21.1	1.882	3.543
InSb	24.4	23.0	1.065	1.134
ZnSe	31.4	26.4	1.188	1.411
InAs	29.0	26.7	1.088	1.185
GaAs	35.4	33.3	1.063	1.131
InP	42.7	38.1	1.121	1.256
GaP	46.8	45.4	1.030	1.061
MgO	89.8	49.8	1.805	3.260
MgF_2	81.6	55.8	1.462	2.138
GaN	92.6	69.5	1.332	1.775
Al_2O_3	141.2	70.6	2.000	4.000
AlN	111.0	83.4	1.332	1.774
SiC	104.1	95.0	1.095	1.200
BN	161.9	130.9	1.237	1.530

Table S1. *The LO and the TO modes of some common materials, along with the ratios* ω_{LO}/ω_{TO} *and* $\varepsilon_{st}/\varepsilon_{\infty}$ *revealing the validity of Lyddane-Sachs-Teller relationship.*

9. Multi-oscillator optimization for SPhP materials with LST constraints

In the main text, we claim that the optimal SPhP material is one with a single optical phonon transition at the optimal frequency. In this section, we provide detailed analysis for this argument and show how this single-oscillator result comes from numerical experiments without prescribing any limit to the number of oscillators or oscillator frequencies.

In this analysis, we consider all possible SPhP materials that satisfy causality and the Lyddane-Sachs-Teller (LST) constraints. Depending on the lattice structures, material susceptibilities can have several optical phonon modes. For example, SiO_2 has several optical phonon bands in the infrared regime, each with significant contributions to HTC. Would more oscillators mean larger response in HTC? How many oscillators are optimal? Also, would the optimal frequency be different if there are more than one oscillators?

To represent any causality-allowed permittivity, we follow the approach in Ref. [16], as discussed in the main text, and write any SPhP material permittivity as a sum of Drude-Lorentz oscillator,

$$\varepsilon(\omega) = 1 - \sum_{i=1}^{N} \frac{\omega_{\mathrm{p},i}^2}{\omega^2 - \omega_i^2 + i\omega\gamma_i}$$

where $\omega_{\mathrm{p},i}^2 \equiv c_i$ are the squared oscillator amplitudes. With a large enough number of oscillators, one can represent any possible material permittivity with this form. To optimize over all possible permittivities, then, one can do the following: choose a dense grid of oscillator frequencies along the real line. An appropriately small loss rate should be paired with each frequency. (Details of how this choice can be made are given in Ref. [16].) The only degrees of freedom, then, are the coefficients, $c_i = \omega_{p,i}^2$. One can optimize over these coefficients using any gradient-based optimization techniques (below we use a modified version of gradient descent), with sufficiently many different starting points to see if a global optimum emerges.

For realistic SPhP materials, we must impose the LST relation as an additional constraint on the coefficients in the permittivity representation. Taking the ratio of (phonon-contributed) static and high-frequency dielectric constants to be bounded above by 4 implies that the coefficients in the permittivity representation must satisfy $\sum_i \frac{c_i}{\omega_i^2} \leq 3$. There is in fact another implicit constraint that must be satisfied as well: that all coefficients remain nonnegative throughout the optimization. How can one incorporate these constraints into a gradient-based algorithm?

Notationally, we bundle the oscillator strengths c_i into a vector $\boldsymbol{c}$, of size $N \times 1$ for N oscillators. We create a second vector $N \times 1$ vector $\boldsymbol{v}$ whose elements are given by $\frac{1}{\omega_i^2}$. We start the optimization with a randomly chosen vector $\boldsymbol{c_0}$ that satisfies the equality version of the LST constraint. (We can assume the solution will satisfy the equality LST relation; otherwise, it would represent an "inactive" constraint and the SPhP optimum would be the same as the Drude-allowed optimum, which of course it cannot be.) At each iteration, we compute the gradient, $\boldsymbol{g} = \partial(HTC)/\partial\boldsymbol{c}$, of the HTC with respect to $\boldsymbol{c}$ (details given below of how to compute the gradient). We want to find a "step," $\Delta\boldsymbol{c}$, roughly in the direction of the gradient, but simultaneously respect the equality LST constraint and the positive constraint. We form a linear program to meet each of these objectives:

$$\min_{\Delta c}(-\boldsymbol{g}^T \Delta\boldsymbol{c})$$

$$\text{s.t. } \boldsymbol{v}^T \Delta\boldsymbol{c} = 0$$

$$0 \leq \boldsymbol{c}_0 + \Delta\boldsymbol{c}$$

$$\|\Delta \boldsymbol{c}\|_1 \leq b.$$

The objective promotes large overlap with the gradient (and hence the maximum possible increase in HTC for a given step size). The first constraint enforces the LST condition, while the second enforces the positivity constraint. The last is a "box" constraint that ensures small steps are taken, for which the gradient will be a good approximation of the HTC function across the design landscape. We perform many iterations (up to 100) and find that the optimizations always converge to a single-oscillator solutions. (Or, due to discretization, two neighboring nonzero oscillators with all others zero.)

Before showing the results of the optimization, we provide more details of how to compute the gradient:

$$g_i = \frac{\partial \mathrm{HTC}}{\partial c_i} = \frac{1}{4\pi^2} \int_0^\infty \mathrm{d}\omega \, \frac{\partial \Theta(\omega, T)}{\partial T} \int_0^\infty \mathrm{d}\beta \, \frac{\partial \xi(\omega, \beta)}{\partial c_i},$$

where β is the wavevector component parallel to the gap surface, and $\xi(\omega, \beta)$ is the modal photon exchange:

$$\xi(\omega, \beta) = \frac{4(\mathrm{Im}\, r)^2 e^{2ik_{0,z}d}}{|1 - r^2 e^{2ik_{0,z}d}|^2},$$

where $r(\omega, \beta) = \frac{k_{0,z}\varepsilon - k_{1,z}}{k_{0,z}\varepsilon + k_{1,z}}$ is the reflectivity and $k_{j,z} = \sqrt{\varepsilon_j \frac{\omega^2}{c^2} - \beta^2}$ is z-component of the wavevector inside the vacuum gap ($j = 0$) and inside the ε_1 material ($j = 1$). We perform the integration numerically for each element of the gradient vector.

To showcase the result, we use temperature $T = 300$ K and gap separation $d = 50$ nm, but our findings generalize to any temperature and near-field gap separation of interest. We observe in the optimization process that the numerical gradients usually favor smaller frequency oscillators (i.e., Drude-like responses), but the imposition of the total LST constraint tends to push the optimal solutions to higher frequencies. The optimization always evolves to a single nonzero oscillator strength, at the same oscillator frequency that is optimal if one only optimizes the strength, frequency, and loss rate of a single Drude-Lorentz oscillator. For the 300K temperature and 50nm gap-separation case, this optimal oscillator has a frequency close to $\omega_{\mathrm{TO},i} = 0.045$ eV and an amplitude $\omega_{\mathrm{p},i} = \sqrt{3}\omega_{\mathrm{TO},i}$, corresponding to $\omega_{\mathrm{LO}} = 2\omega_{\mathrm{TO}}$, with an optimal HTC of $5400\ \mathrm{Wm^{-2}K^{-1}}$.

Figure S8 shows the initial (blue circles) and optimal (red circles) oscillator distribution of an example optimization, as well as the improvement in HTC values through all iterations.

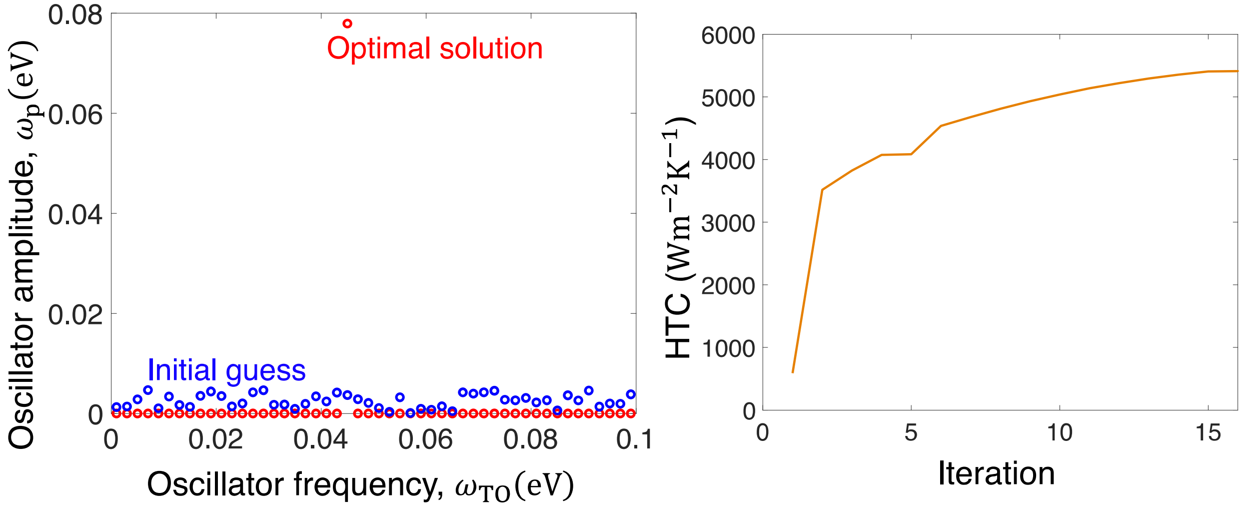

Figure S8. *Multiple-oscillator optimization of HTC with LST constraints. The setup is temperature $T = 300\ K$ and the gap separation $d = 50\ nm$. (a) Initial (blue) and optimal (red) oscillator distribution. (b) HTC values at each iteration.*

10. Temperature and loss rate dependence of optimal SPhP materials

How do the optimal SPhP material properties depend on the temperature for NFHRT? The optimization approaches we used can be easily generalized to any other temperature. For any temperature, the optimal response again emerges as a single Drude-Lorentz oscillator at an optimal frequency ω_{TO} which scales linearly with temperature. In Figure S9 we show the optimal frequencies and the corresponding optimal HTC values for temperatures in the range 100 K to 2000 K. The linear dependence of the optimal oscillator frequency on the temperature is analogous to Wien's Law, for far-field radiation, but with a different scaling constant (as shown in the main text of Ref. [16], and which emerges here in the SPhP case). The linear scaling of the optimal HTC as a function of temperature is a unique feature of the near field (far-field blackbody HTC scales as the cube of temperature). It emerges from the combination of the fact that the Planck function peaks at zero frequency, while near-field local density of states must satisfy an all-frequency sum rule. Our optimizations confirm these intuitions.

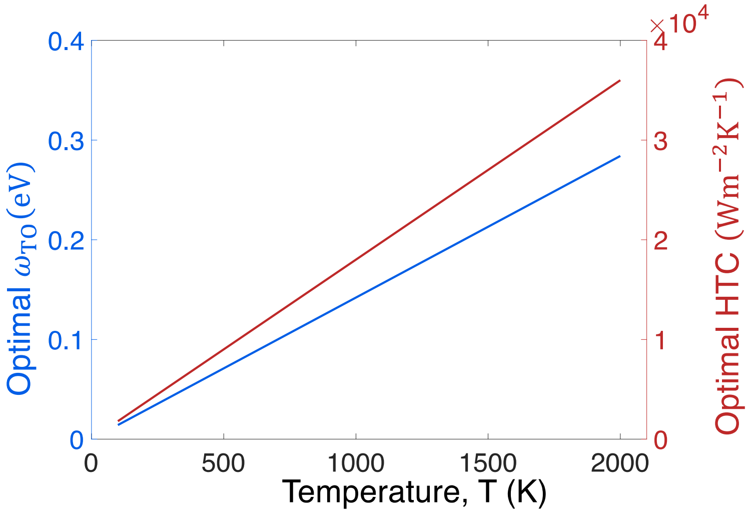

Figure S9. *Temperature dependence of optimal oscillator frequency (blue) and the corresponding optimal HTC (red).*

How does the loss rate γ affect the optimal material choice and maximal HTC? Fundamentally, the loss rate plays very little part in the resonance condition and therefore does not affect the optimal resonance frequency for NFRHT. Figure S10 shows the optimal oscillator frequency ω_{TO} and optimal HTC for a range of material loss rates (normalized by oscillator amplitude ω_{p}). The optimal ω_{TO} (blue curve) is essentially constant. In terms of optimal HTC, it can only be affected by loss rate to a limited degree. As illustrated in Figure S10, except for extremely small loss rates, the peak HTC (red curve) is relatively robust as a function of loss rates.

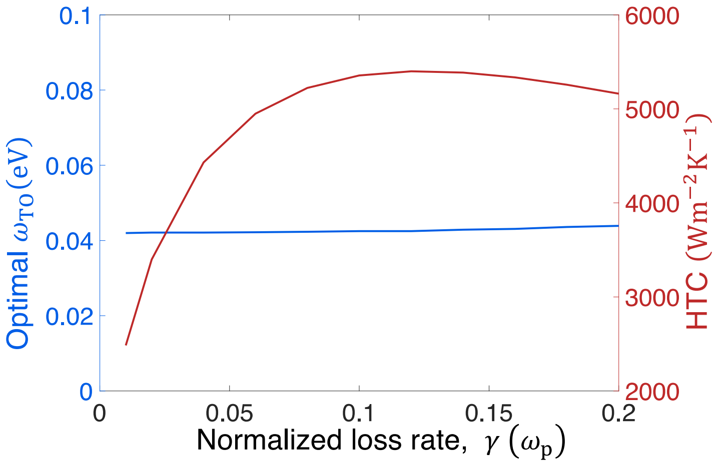

Figure S10. Optimal oscillator frequency ω_{TO} (blue) and optimal HTC (red) for different material loss rates γ, where γ is normalized by oscillator amplitude ω_{p}.

References

1. Yeh, P. Optical waves in layered media. *New York: Wiley* **1988**.
2. Biehs, S. A., Ben-Abdallah, P., Rosa, F. S. S., Joulain, K., Greffet, J. J. Nanoscale heat flux between nanoporous materials. *Opt. Express* **2011**, *19* (19), A1088-A1103.
3. Liu, M. C., Lee, C. C., Kaneko, M., Nakahira, K. & Takano, Y. Microstructure of magnesium fluoride films deposited by boat evaporation at 193 nm. *Appl. Optics* **2006**, 45, 7319-7324.
4. Dumas, L., Quesnel, E., Robic, J. Y. & Pauleau, Y. Characterization of magnesium fluoride thin films deposited by direct electron beam evaporation. *J. Vac. Sci. Technol. A* **2000**, 18, 465-469.
5. Miikkulainen, V., Leskela, M., Ritala, M. & Puurunen, R. L. Crystallinity of inorganic films grown by atomic layer deposition: Overview and general trends. *J. Appl. Phys.* **2013**, 113, 021301.
6. Walsh, R. B. *et al.* Model Surfaces Produced by Atomic Layer Deposition. *Chem. Lett.* **2012**, 41, 1247-1249.
7. Song, B. *et al.* Enhancement of near-field radiative heat transfer using polar dielectric thin films. *Nat. Nanotechnol.* **2015**, 10, 253-258.
8. Basu, S. & Zhang, Z. M. Ultrasmall penetration depth in nanoscale thermal radiation. *Appl. Phys. Lett.* **2009**, 95, 133104.
9. Francoeur, M., Menguc, M. P. & Vaillon, R. Near-field radiative heat transfer enhancement via surface phonon polaritons coupling in thin films. *Appl. Phys. Lett.* **2008**, 93, 043109.
10. Palik, E. D. Handbook of optical constants of solids. (Academic Press, San Diego, **1998**).
11. Barker, A. S., Long-Wavelength Soft Modes, Central Peaks, and Lyddane-Sachs-Teller Relation. *Phys. Rev. B.* **1975,** *12* (10), 4071-4084.
12. Chang, I. F.; Mitra, S. S.; Plendl, J. N.; Mansur, L. C., Long-Wavelength Longitudinal Phonons of Multi-Mode Crystals. *Phys. Status Solidi.* **1968,** *28* (2), 663-673.
13. Shur, M. S. *et al.* Handbook Series on Semiconductor Parameters - Volume 1: Si, Ge, C (Diamond), GaAs, GaP, GaSb, InSs, InS, InSb. (World Scientific Publishing Company, **1999**).
14. Barker, A. S. Transverse and Longitudinal Optic Mode Study in MgF_2 and ZnF_2. *Phys. Rev.* **1964**, 136, 1290-1295.
15. Madelung, O. Semiconductors : data handbook, 3rd Edn. (Springer, Berlin, **2004**).
16. Zhang, L.; Miller, O. D. Optimal Materials for Maximum Large-Area Near-Field Radiative Heat Transfer. *ACS Photonics* **2020**, *7* (11), 3116-3129.